# Epitaxial graphene morphologies probed by weak (anti)-localization

Ather Mahmood, Cécile Naud, Clément Bouvier, Fanny Hiebel, Pierre Mallet, Jean-Yves Veuillen, Laurent Lévy, Didier Chaussende, Thierry Ouisse

# Epitaxial graphene morphologies probed by weak (anti)-localization

A. Mahmood, C. Naud,* C. Bouvier, F. Hiebel, P. Mallet, J.-Y. Veuillen, and L. P. Lévy†

*Institut Néel, CNRS and Université Joseph Fourier,*

*BP 166, 38042 Grenoble Cedex 9, France*

D. Chaussende and T. Ouisse

*Laboratoire des Matériaux et du Génie Physique, CNRS UMR5628 - Grenoble INP,*

*Minatec 3 parvis Louis Néel, BP257, 38016 Grenoble, France*

## Abstract

We show how the weak field magneto-conductance can be used as a tool to characterize epitaxial graphene samples grown from the C or the Si face of Silicon Carbide, with mobilities ranging from 120 to 12000 $cm^2/(V.s)$. Depending on the growth conditions, we observe anti-localization and/or localization which can be understood in term of weak-localization related to quantum interferences. The inferred characteristic diffusion lengths are in agreement with the scanning tunneling microscopy and the theoretical model which describe the "pure" mono-layer and bilayer of graphene [MacCann *et al*,. Phys. Rev. Lett. **97**, 146805 (2006)].

*Electronic address: cecile.naud@grenoble.cnrs.fr

†Electronic address: laurent.levy@grenoble.cnrs.fr

## I. INTRODUCTION

Considerable progress has been achieved in the synthesis of two-dimensional graphene. Since the seminal works [1, 2] which used exfoliated graphite flakes transferred onto $SiO_2$ substrates, full wafers of epitaxial graphene can now be grown by high temperature graphitization of Silicon Carbide (SiC) crystals starting either from their Carbon or Silicon face [3]. More recently, MBE growth on SiC substrate have been achieved [4] and CVD synthesis of large area graphene films have also been carried out on the surface of transition metals in high vacuum [5] or at ambient pressure [6, 7]. The subsequent transfer of such CVD graphene films to a large variety of substrates is now controlled. These synthesis methods are scalable and offer some real perspectives for micro-electronic applications. A number of characterization techniques are available for the grown layers: STM, AFM, Raman, TEM/SEM and photo-emission have proven their usefulness. On the other hand, the relationship between the growth conditions, the film morphologies and the electronic properties have not yet been systematically investigated [8–16]. This correlation is important since epitaxial graphene presents characteristic defaults which differentiates it from the "pure" free graphene.

In this paper, low field magneto-resistance is used to correlate the transport properties, the growth conditions and the morphologies of epitaxially-grown graphene films elaborated from the different surfaces of 6H-SiC. The films studied have been grown with different graphene layer numbers, both from the Si and C terminated faces, some in ultra-high vacuum other in inert atmospheres. Depending on the SiC polytype and on the growth conditions, distinct surface morphologies can be observed which lead to very different magnetoresistance behaviors (see figure 1). Exploiting the unique features of interference phenomena present in magneto-transport, electronic properties can be related to the surface morphologies.

## II. LOCALIZATION AND ANTI-LOCALIZATION IN GRAPHENE

Low field magneto-resistance is a sensitive probe for electronic transport as it measures the effect of quantum interferences along closed paths [17–19]. Depending on the closed loop size, the interferences can be constructive or destructive. For very small loops, it has been demonstrated both theoretically [20, 21] and experimentally [22, 23] that inter-

ferences between identical time reversed paths are destructive in graphene leading to a negative magnetoconductance (positive magnetoresistance), which is characteristic of anti-localization of electron waves. For graphene, electron wavefunctions have four components and may be characterized by two additional quantum numbers: the isospin and the pseudospin. The isospin measures the relative wavefunction amplitude on the equivalent sites (A-B) in graphene unit cell, while the pseudospin measures to which band valley $K+$ or $K-$ the quantum states belong [24]. Antilocalization is a characteristic feature of graphene as the isospin (collinear to momentum) undergoes a full rotation on a closed loop, changing the wavefunction sign and so forbidding the backscattering. As the loop size increases, scattering mechanisms lead to additional rotations of the isospin, as well as to the scattering between different valley states, such that the pseudospin need not be preserved on long paths. Two lengthscales characterize this diffusion: the pseudospin is controlled by the intervalley diffusion length $L_i$, and $L_*$ the intravalley diffusion length controls the isospin random diffusion. The "overall" effect of these processes on the interferences along time-reversed paths is to change their sign back to the "normal" positive magneto-conductance due to coherent backscattering [20, 21] observed in other two-dimensional systems. Eventually, for extremely long paths (of length greater then $L_\varphi$, the phase coherence length) and/or high temperatures, inelastic scattering kills interferences. The beauty of quantum interference is that a characteristic magnetic field can be associated to every loop size, when half a flux quantum is threaded within the loop area: hence the magnetic fields $B_{\varphi,i,*} = \frac{\Phi_0}{4\pi L^2_{\varphi,i,*}}$ can be associated to the lengthscales $L_{\varphi,i,*} = \sqrt{D\tau_{\varphi,i,*}}$ respectively.

It is useful to recall some of the general features of epitaxial graphene on SiC. Graphene layers can be grown by Si sublimation at high temperature [25]. Electrical conduction is known to be dominated by the completed layers closest to the interface [26]. When growing from the SiC C-face, there is a rotation between successive layers which effectively decouples

TABLE I: Characteristics and extracted parameters of the epitaxial samples studied.

| Face | growth | layer # | $\mu(\mathrm{m}^2/(\mathrm{V\cdot s})$ | $\mathrm{D}(\mathrm{m}^2/\mathrm{s})$ | $L_\varphi$(4K) | $L_i$ | $L_*$ |
|---|---|---|---|---|---|---|---|
| C | UHV | $\leq 5$ | 0.018 | 0.0025 | 72 nm | 40 nm | 26 nm |
| C | Ar | $\approx 50$ | 1.2 | 0.159 | 740 nm | | |
| Si | UHV | 2 | 0.012 | 0.0022 | 140 nm | 30 nm | 18 nm |

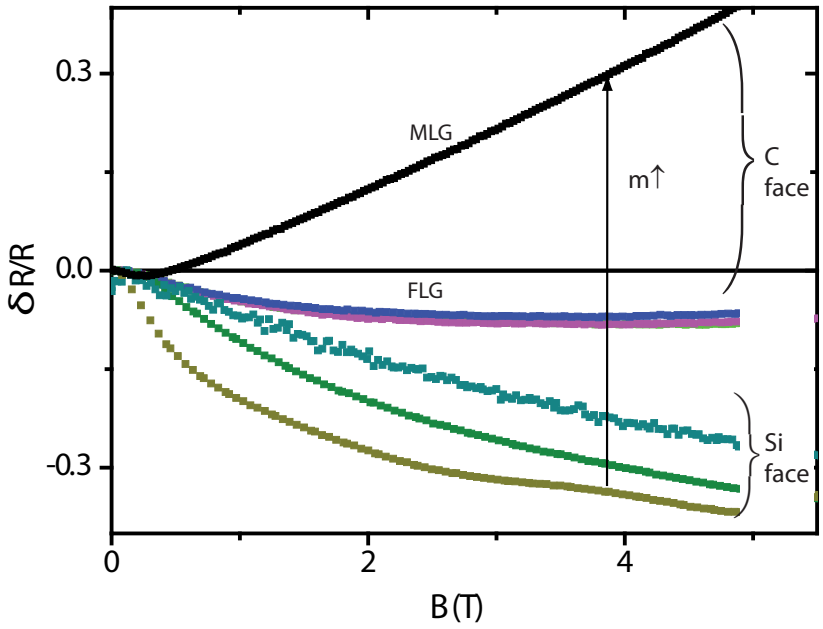


FIG. 1: Overview of the magnetoresistance traces on a large field scale (5T) of 6 graphene epitaxial samples grown in different conditions and measured at 4K. A positive magnetoresistance is observed for the highest mobility (m) samples (grown from the SiC C-face), with different slopes for few layers (FLG) (number of layers $< 10$) and multilayer (MLG) (number of layers $>> 10$) graphene, while negative magnetoresistance are observed on samples grown from the SiC Si-face. All these traces are analyzed quantitatively in this paper and related to the surface morphology.

the layers [27, 28]. This is to be contrasted from graphene layers grown from the Si face, where Bernal stacking breaks the symmetry between the two (A-B) carbon sites [25]. In both cases, completed layers are continuous and ripples cover the SiC vicinal steps. Depending on the growth condition, folds are also observed. On ripples or folds, there is a local stretching of the graphene bonds. The other types of known defects arise at the graphene/SiC interface. Defects far from the graphene layer (at distance $d \gg a$, where $a$ is graphene lattice constant) do not break the A-B symmetry and contribute only to intravalley elastic scattering. Sharp potential variations ($d \approx a$), may break the graphene A-B symmetry locally. This scattering potential is time-reversal even and affects simultaneously the isospin and pseudospin and contribute both to the inter and intravalley scattering [20, 21]. Ripples and folds stretch bonds and contribute equally to inter and intra valley scattering. Finally, trigonal warping contributes only to intravalley scattering [20, 21].

These scattering processes govern the crossover from localization at low field to anti-localization at high field. The quantum correction [20, 21] to the magneto-conductance $\delta G^{mono} = \delta G_i + \delta G_*$ of a single graphene layer can be split between the intervalley

$$\delta G_i = \frac{e^2}{\pi\hbar}\left[F\left(\frac{B}{B_\varphi}\right) - F\left(\frac{B}{B_\varphi + 2B_i}\right)\right] \quad (1)$$

and the intravalley contributions

$$\delta G_* = -\frac{2e^2}{\pi\hbar}\left[F\left(\frac{B}{B_\varphi + B_i + B_*}\right)\right], \quad (2)$$

where the function $F(x) = \ln(x) + \Psi(1/2 + 1/x)$, and $\Psi$ is the digamma function.

When the A-B symmetry is fully broken (for a bilayer on Si face, the two sublattices A and B are no more equivalent) the intravalley contributions have the opposite sign $\delta G^{bi} = \delta G_i - \delta G_*$: the magnetoconductance increases monotonously with field and antilocalization disappears [20, 21].

## III. RESULTS AND DISCUSSION

Figure 1 gives an overview of all the magnetoresistance behaviors observed at 4K over a broader range of magnetic field. The transport properties have been measured using contacts pads evaporated through a mask with a Van der Paw geometry (surface of $500\mu m^2$). Four points DC measurements were performed down to $4.2K$. Films grown from the SiC C-face have larger mobilities and positive magnetoresistance at high fields. Thick films grown from the C-face (top trace) show a linear magnetoresistance at larger fields. The positive magnetoresistance observed at high field for SiC C-face samples can be contrasted with the SiC Si-face graphene which have lower mobilities and a negative magnetoresistance at all fields.

These differences can be understood in terms of weak localization and anti-localization in graphene. Using the appropriate weak-localization formulae, the intervalley, intravalley and phase coherence length can be obtained by fitting the magnetoconductance curves. All the results are summarized in table I and are discussed in the rest of this article.

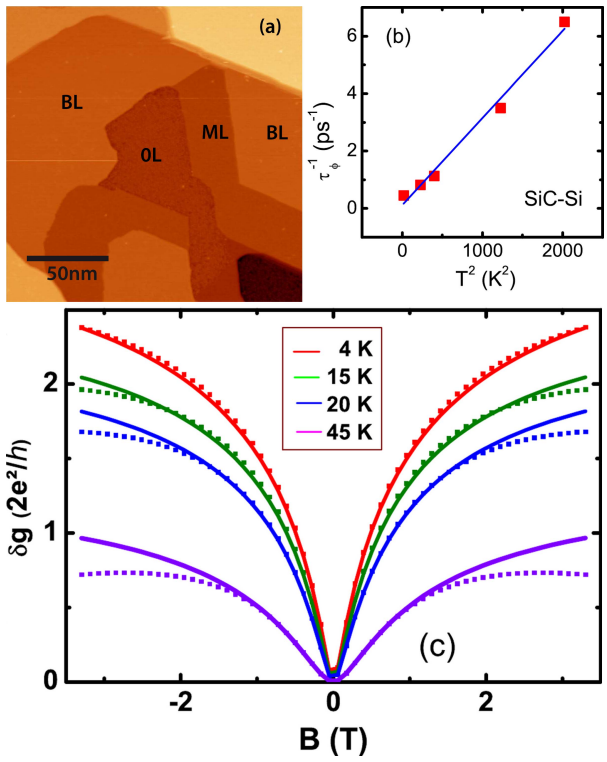


FIG. 2: Graphene sample grown from the SiC Si-face. Top left (a): STM topographic image showing the terraces with different numbers of graphene layers (the labelling as ML for monolayer, BL for bilayer is inferred from the step-height[29]). The average number of layers for this sample is of the order 2 (bilayer). Top right (b): The temperature dependence of the phase coherence length given by the the weak localization fits. The quadratic dependence observed suggests a phonon-dominated dephasing process. Bottom (c): Bilayer magnetoconductance measured at different temperatures (continuous line). The magneto-conductance increases monotonously with field at low $T$: it fits the expected quantum correction to the conductance when the A-B symmetry is broken (dashed line).

### A. Magneto-conductance on the Si-face of 6H-SiC

We first consider samples grown by graphitization of the SiC Si-face. The growth dynamics is slow and the average number of graphene layers can be controlled. When the number of layers exceeds one, the layers stack as in graphite (Bernal) and break the A-B symmetry. In the STM topographical image shown in Figure 2-a, the domains with different number of layers can be precisely identified and labelled. On average, this sample has $\approx 2$ layers and a mobility of 120 cm$^2$/(V.s). STM studies have shown that the bilayers

cover around 50% of the surface of our sample. The upper graphene layer is continuous over the monolayer-bilayer junction [11]. The electron transmission between monolayer and bilayer graphene has been theoretically studied for zigzag and armchair boundaries. Due to the presence of an evanescent wave in the bilayer graphene, traveling modes are well connected to each other. The transmission through the boundary is strongly dependent on the incident angle [30]. Nevertheless, the experimental measurements at the atomic scale have shown a poor transmission factor of $T = 1/2$ and such junctions of monolayer-bilayer will reduce the macroscopic conductivity [11]. In our sample ,strong intervalley scattering was not observed at the single/bilayer edges in STM studies due to the smooth scattering potential in the continuous surface layer [31]. The magnetoconductance traces plotted in units of $2e^2/h$ for different temperatures are shown in Figure 2-c: the continuous increase observed as a function of field saturates on the scale of $e^2/h$. All curves can be fitted with the weak-localization formulae [20, 21] $\delta G^{bi} = \delta G_i - \delta G_*$ appropriate for bilayers, assuming that the phase coherence length $L_\varphi$ is the only temperature dependent parameter. Despite the fact that the sample is inhomogeneous, we assume that the signal from the majority bilayer areas dominates the weak localization correction [42]. The characteristic field $B_* = 0.935\,\mathrm{T}$ obtained from the fits is close to twice $B_i = 0.44\,\mathrm{T}$. This ratio has been observed in most samples studied. Using $B_*, B_i$, the intervalley $L_i$ and intravalley $L_*$ diffusion lengths are found to be comparable to the size of the flat terraces. This suggests that intervalley and intravalley scattering are dominated by the boundaries between domains. The time-reversed loops thus concern homogeneous domains. The corresponding timescales $\tau_{i,*} = L^2_{\varphi,i,*}/(4D)$ are set by the diffusion coefficient D for this 2D-sample. Using the fits, the dependence of the phase breaking rate $\tau_\varphi^{-1}$ on temperature, is shown in Figure 2-b. The $T^2$ behavior observed should be contrasted with the linear dependence observed for the C-face [22]. A quadratic increase of $\tau_\varphi^{-1}$ has also been observed at high temperatures by Tikhonenko et al. [23]. The linear contribution due to electron-electron dephasing appears to be quenched by the gap induced by Bernal stacking, leaving another scattering mechanism, probably associated with phonons, as the dominant one. For semiconductor 2D electronic systems, the electron-phonon scattering rate is known both from theory and experiments to increase as $T^3$. For isolated graphene planes, different regimes [32] have been identified depending on the relative value of the temperature compared to the Bloch-Grüneisen temperature $T_{BG} = 2k_F v_{\mathrm{ph}}/k_B$ ($\approx 90K$ for this sample): below $T_{BG}$, the rate grows as $T^4$, while it is

linear above [33]. How the SiC substrate affects this behavior is not known. While the fits (Figure 2-c) are quite accurate at low fields, deviations can be observed at high temperature and high fields: a negative component in the magnetoresistance traces grows at large fields as the temperature is raised. The origin of this classical-like behavior is not clear, but it is concomitant with the appearance of the quadratic dephasing rate.

### B. Magneto-conductance on the C-face of 6H-SiC

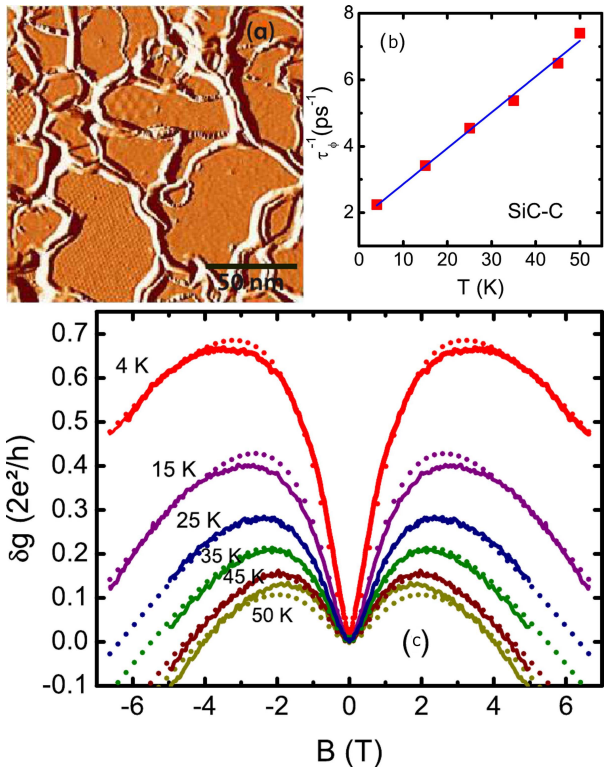


FIG. 3: Graphene sample grown from SiC C-face. Top left (a) : Derivative STM image (200 nm×200 nm) showing the surface morphology of a sample graphitized in UHV. The flat terraces are of the order of 60 nm in size and are separated by ripples and folds. Top right (b): temperature dependence of the dephasing rate on the carbon face. Bottom (c): The magnetoconductance traces of C-face grown samples show a weak localization dip (probing the longest coherent loops) close to zero field and a negative magnetoconductance at higher field (anti-localization for short loops). The crossover regime occurs around the field $B_* \approx 2B_i$. At higher temperature, long loops are cut-off ($L_\varphi$ decreases at higher T) reducing the weak localization contribution at low field. The contrast with the Si face (Fig. 2-c) is quite clear.

Samples grown from SiC C-face have notably different morphologies when grown in high vacuum or in an inert atmosphere. When grown in ultra-high vacuum, flat terraces are relatively small as shown on the topographic STM image (Figure 3-a top-left), typically of order 60 nm with folds and ripples at their boundaries. When grown in an inert atmosphere, the domains (and mobilities) are much larger (see figure 4).

As long as the number of layers is small ($\leq 10$), it is possible to analyze the magneto-conductance in term of the weak localization-antilocalization effects discussed above, in agrement with earlier studies [15, 22, 23]. This is illustrated in the bottom panel of Figure 3-c, where the magnetoconductance traces of a UHV grown sample, scaled in units of $2e^2/h$, are plotted for different temperatures. All traces can be fitted to the weak localization correction discussed in equations 1 and 2. In particular, the weak localization dip observed at low field (i.e. for the longest coherent retrodiffusion loops) turns into a negative magnetoconductance at higher fields (anti-localization for small retrodiffusion loops). The characteristic field $B_* \approx 1.8$ T is found to be nearly twice $B_i \approx 0.72$ T as for the Si-face grown samples. The corresponding intervalley $L_i$ and intravalley $L_*$ diffusion length are also of the order of the size of the flat terraces (see the table I). All traces can be fitted assuming that only $L_\varphi$ varies with temperature. The dependence of the dephasing rate $\tau_\varphi^{-1}$ with $T$ is shown in Figure 3-b. The linear temperature dependence, also observed in Wu et al. [22] is consistent with Altshuler-Aronov prediction for electron-electron interactions [34, 35] $\frac{h}{\tau_\varphi} = \frac{k_B T}{2\pi} \frac{R_\square}{R_K} \ln\left(\frac{\pi R_K}{R_\square}\right)$ with $R_K = h/e^2$ is the quantum resitance and $R_\square$ is the square resistance. The measured slope ($\approx 8 \times 10^{10} \mathrm{s}^{-1}\mathrm{K}^{-1}$) is an order of magnitude larger than the expected value. Similar discrepancies are not uncommon in other semiconducting 2DEG systems. Among the other sources of dephasing, the Coulomb scattering of electrons in different layers have been shown theoretically to be relevant [36]. Electron-phonon scattering may also contribute [32, 33].

### C. Thick graphene sample

We now turn to samples graphitized from the SiC C-face in an inert atmosphere which have significantly different morphologies and transport behaviors. When graphitizing from the SiC C-face, the number of layers increases rapidly and a larger number of graphene layers (of order of 30-50 for the sample studied) is reached in a 10 minutes period. After annealing at high temperature, the sample morphology (as shown in the AFM image 4-inset) shows

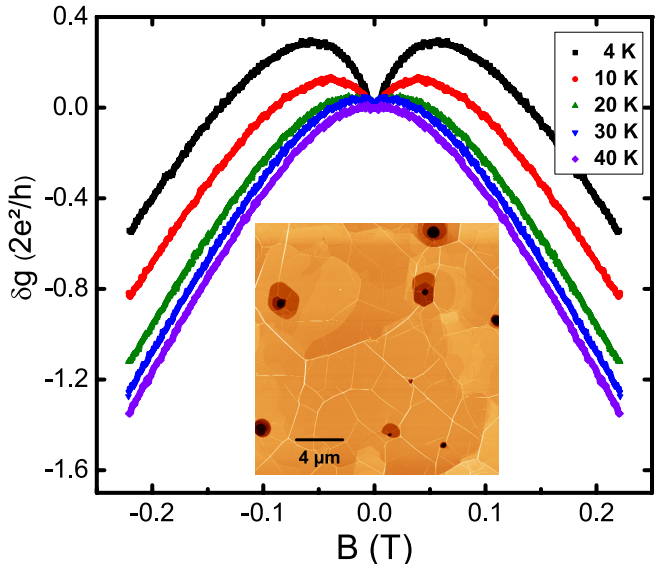


FIG. 4: Magneto-conductance of a thick graphene stack, annealed at high temperature. A narrow weak localization dip close to zero field is observed at low temperature. Above 0.05 T, the negative magnetoconductance cannot be attributed to weak-localization alone. The data is consistent with classical reduction of the longitudinal conductance for electron with relativistic dynamics. Inset: AFM image of the sample showing large (several microns) domains separated by ripples. The holes (black dots) are about 30-40 nm deep.

very large (several $\mu$m) domains separated by fold or ripples. The magnetoconductance traces measured at different temperatures are shown in Figure 4. A narrow weak localization dip close to zero field is clearly seen: its width is controlled by the phase coherence length $L_\varphi$ (of the order of 750 nm at 4 K). The diffusion coefficient (1600 cm$^2$/s) and mobilities ($10^4$cm$^2$/(V.s)) are also found to be much larger than in the UHV grown samples.

Within this thick sample, the conduction is no longer limited to the layer closest to the interface with the SiC. From the measured value of the diffusion coefficient, we infer a large mean free path $\ell_e \approx 300nm$ which comparable to $L_\varphi$. For the semi-classical theory, the curvature of electron trajectories usually results in a positive quadratic magneto-resistance and so a negative magneto-conductance : $\sigma_{xx} = \frac{\sigma_0}{1+(\omega_c\tau_L)^2}$ with $\sigma_0$ the conductivity without magnetic field and $\omega_c = v_F\sqrt{2(\frac{e}{\hbar})B}$ the relativistic graphene cyclotron frequency. A fit to the magnetoconductance shown in Fig. 4 gives a scattering time $\tau_L \approx 0.05$ps shorter than the mean-free time $\tau_e \approx 0.3$ps suggesting other scattering processes are at play in a magnetic field (Coulomb scattering between layers [36], tunneling between graphene plane) which con-

tribute to the broadening of Landau levels and shorten the effective scattering times. The amplitude of the negative magnetoconductance above 0.05 T shown in Fig. 4 also exceeds $e^2/h$ and cannot be attributed to quantum interference alone. Assuming relativistic electron dynamics, the cyclotron radius $r_c = v_F/\omega_c = \ell_B/\sqrt{2}$ becomes smaller than the mean free path for fields exceeding ($B_c \approx 10^{-1}$ T). As seen in Fig. 4, the magnetoconductance turns negative above 0.05 T ($> B_c$). At larger field($> 0.4T$), a linear magnetoresistance regime is observed (the top curve in Fig. 1), which is consistent with previous transport measurements on epitaxial graphene [37]. Several routes to linear magnetoconductance have been previously considered. For inhomogeneous and disordered materials, a classical resistor network model [38, 39] accounts for the linear magnetoresistance observed in silver chalcogenides. Another mechanism leading to a linear magnetoconductance has been considered by Abrikosov[40, 41] for layered materials and small (and zero) gap 3d-semiconductors: in the quantum limit, when the temperature and Fermi energy are smaller than the Landau band splitting, the magnetoresistance becomes linear. For a pure 2d system, the requirements for quantum linear magnetoresistance coincide with the quantum Hall regime. On these samples, the onset of the linear regime (0.5 T) which coincides approximatively to $\omega_c\tau_L \geq 1$ occurs well before the Shubnikov-de Haas oscillations are observed [43]. This indicates that tunneling between layers is larger in these thick graphene samples compared to the few layer samples (number of layers $< 10$. This makes the Abrikosov mechanism the most probable explanation for the linear magnetoresitance, in agreement with Ref.[37]. From a device point of view, the transport characteristics of such thick graphene stack are good. Gating effects measured on such thick graphene stacks have however been found to be small.

### D. Discussion of the intravalley versus intervalley scattering length

The quasiparticles of graphene can be described in the space of four-component wave functions, $|A\rangle_{K+}, |B\rangle_{K+}, |B\rangle_{K-}, |A\rangle_{K-}$ basis describing electronic amplitude on $A$ and $B$ sites and in the valleys $K+$ and $K-$. In order to describe the microscopic scattering potentials, we introduce two sets of $4X4$ hermitian matrices : the isospin ($\vec{\Sigma} = (\Sigma_x, \Sigma_y, \Sigma_z)$) and the pseudospin ($\vec{\Lambda} = (\Lambda_x, \Lambda y, \Lambda_z)$) [20, 21]. Then the electron hamiltonian in weakly disorder graphene can be parameterized as

$$V(\vec{r}) = u_0(\vec{r})\hat{\mathbf{I}} + \sum_{i,j} u_{i,j}(\vec{r})\Lambda_i\Sigma_j(i,j \equiv x,y,z) \tag{3}$$

For each scattering potential $u_{i,j}(\vec{r})$, there is a microscopic scattering rate $\tau_{ij}^{-1}$. Since $x$ and $y$ are equivalent ($\perp$), there are only four microscopic scattering rates, $\tau_{zz}^{-1}, \tau_{z\perp}^{-1}, \tau_{\perp z}^{-1}$ and $\tau_{\perp\perp}^{-1}$. If the sample is sufficiently disordered, it is plausible to assume that all the potential $u_{ij}$ and scattering rates $\tau_{ij}^{-1}$ are comparable. In this limit, the inter and intravalley scattering rates [21] $\tau_i^{-1} = 4\tau_{\perp\perp}^{-1} + 2\tau_{z\perp}^{-1} \approx 6\tau_0^{-1}$ and $\tau_*^{-1} = \tau_i^{-1} + 2\tau_z^{-1} \approx 12\tau_0^{-1}$ since $\tau_z = 2\tau_{zz}^{-1} + \tau_{\perp z}^{-1}$. $B_* = \frac{\Phi_0}{4\pi D\tau_*}$ is found to be twice $B_i = \frac{\Phi_0}{4\pi D\tau_i}$ in agreement with our experimental results, and the weak localization correction depends only on $B_*$ as $B_\varphi \overset{T\to 0}{\longrightarrow} 0$: there is a universal scaling of the magnetoconductance in $B/B_*$ and all samples-magnetoconductances collapse on this curve at low temperatures.

## IV. CONCLUSIONS

In this paper, an overview of weak localization properties on a variety of epitaxially grown samples has been presented. For all types of few-layers graphene samples, the measured characteristic lengthscales for iso and pseudo-spin diffusion (intra/intervalley scattering) coincide with the terrace and or domain sizes identified on the samples by STM or AFM images. For most samples, the magnitude of the intervalley and intravalley scattering rates have a ratio of 2. Such a ratio is found when all scattering rates $\tau_{ij}^{-1}$ induced by the scattering potentials (cf. Eq. 3) $\tau_{ij}^{-1}$ $(i,j \equiv, z, \perp)$ are of similar magnitude. The propagation through a domain is ballistic $l_e = V_F\tau_e$ and most of the diffusion occurs at the edge of the terraces where all types of scattering processes are present. In the case of thick samples grown in furnace, the elastic mean free path is smaller than the domains' size and the propagation through a domain is no more ballistic but diffusive. Other scattering processes are involved like coulomb scattering between layers or tunneling between graphene plane.

### Acknowledgments

We acknowledge L. Magaud for her critical reading of this article. This work is supported by the French National Research Agency (GraphSiC and XPgraphene projects) and the

Nanosciences Foundation (DISPOGRAPH project).

---

[1] K. S. Novoselov, A. K. Geim, S. V. Morozov, D. Jiang, M. I. Katsnelson, I. V. Grigorieva, S. V. Dubonos, and A. A. Firsov, Nature **438**, 197 (2005).

[2] Y. B. Zhang, Y. W. Tan, H. L. Stormer, and P. Kim, Nature **438**, 201 (2005).

[3] C. Berger, Z. M. Song, T. B. Li, X. B. Li, A. Y. Ogbazghi, R. Feng, Z. T. Dai, A. N. Marchenkov, E. H. Conrad, P. N. First, and W. A. de Heer, Journal of Physical Chemistry B **108**, 19912 (2004).

[4] E. Moreau, F. J. Ferrer, D. Vignaud, S. Godey, and X. Wallart, Physica Status Solidi a-Applications and Materials Science **207**, 300 (2010).

[5] J. Coraux, A. T. N'Diaye, C. Busse, and T. Michely, Nano Letters **8**, 565 (2008).

[6] K. S. Kim, Y. Zhao, H. Jang, S. Y. Lee, J. M. Kim, K. S. Kim, J. H. Ahn, P. Kim, J. Y. Choi, and B. H. Hong, Nature **457**, 706 (2009).

[7] X. S. Li, W. W. Cai, J. H. An, S. Kim, J. Nah, D. X. Yang, R. Piner, A. Velamakanni, I. Jung, E. Tutuc, S. K. Banerjee, L. Colombo, and R. S. Ruoff, Science **324**, 1312 (2009).

[8] J. A. Robinson, M. Wetherington, J. L. Tedesco, P. M. Campbell, X. Weng, J. Stitt, M. A. Fanton, E. Frantz, D. Snyder, B. L. VanMil, G. G. Jernigan, R. L. Myers-Ward, C. R. Eddy, and D. K. Gaskill, Nano Letters **9**, 2873 (2009).

[9] T. Low, V. Perebeinos, J. Tersoff, and P. Avouris, Phys. Rev. Lett. **108**, 096601 (2012).

[10] S. Tanabe, Y. Sekine, H. Kageshima, M. Nagase, and H. Hibino, Applied Physics Express **3**, 075102 (2010).

[11] S.-H. Ji, J. B. Hannon, V. Tromp, R. M .and Perebeinos, J. Tersoff, and F. M. Ross, Nature Materials **11**, 114 (2011).

[12] Y.-M. Lin, C. Dimitrakopoulos, D. B. Farmer, S.-J. Han, Y. Wu, W. Zhu, D. D. Kurt Gaskill, J. L. Tedesco, R. L. Myers-Ward, C. R. Eddy, A. Gril, and P. Avouris, Applied Physics Letters **97**, 112107 (2010).

[13] K. Lee, S. Kim, M. S. Points, T. E. Beechem, T. Oht, and E. Tutuc, NanoLetters **11**, 3624 (2011).

[14] J. Jobst, D. Waldmann, F. Speck, R. Hirner, D. K. Maude, T. Seyller, and H. B. Weber, Phys. Rev. B **81**, 195434 (2010).

[15] G. L. Creeth, A. J. Strudwick, J. T. Sadowski, and C. H. Marrows, Phys. Rev. B **83**, 195440 (2011).

[16] S. Lara-Avila, A. Tzalenchuk, S. Kubatkin, R. Yakimova, T. J. B. M. Janssen, K. Cedergren, T. Bergsten, and V. Fal'ko, Phys. Rev. Lett. **107**, 166602 (2011).

[17] G. Bergmann, Solid State Communications **42**, 815 (1982).

[18] G. Bergmann, Physics Reports-Review Section of Physics Letters **107**, 1 (1984).

[19] B. L. Altshuler, D. Khmel'nitzkii, A. I. Larkin, and P. A. Lee, Physical Review B **22**, 5142 (1980).

[20] E. McCann, K. Kechedzhi, V. I. Fal'ko, H. Suzuura, T. Ando, and B. L. Altshuler, Physical Review Letters **97**, 146805 (2006).

[21] K. Kechedzhi, E. McCann, V. I. Fal'ko, H. Suzuura, T. Ando, and B. L. Altshuler, European Physical Journal-Special Topics **148**, 39 (2007).

[22] X. S. Wu, X. B. Li, Z. M. Song, C. Berger, and W. A. de Heer, Physical Review Letters **98**, 136801 (2007).

[23] F. V. Tikhonenko, A. A. Kozikov, A. K. Savchenko, and R. V. Gorbachev, Physical Review Letters **103**, 226801 (2009).

[24] A. H. Castro Neto, F. Guinea, N. M. R. Peres, K. S. Novoselov, and A. K. Geim, Reviews of Modern Physics **81**, 109 (2009).

[25] J. Hass, W. A. de Heer, and E. H. Conrad, Journal of Physics-Condensed Matter **20**, 323202 (2008).

[26] C. Berger, Z. M. Song, X. B. Li, X. S. Wu, N. Brown, C. Naud, D. Mayou, T. B. Li, J. Hass, A. N. Marchenkov, E. H. Conrad, P. N. First, and W. A. de Heer, Science **312**, 1191 (2006).

[27] J. Hass, F. Varchon, J. E. Millan-Otoya, M. Sprinkle, N. Sharma, W. A. De Heer, C. Berger, P. N. First, L. Magaud, and E. H. Conrad, Physical Review Letters **100**, 125504 (2008).

[28] C. Faugeras, A. Nerriere, M. Potemski, A. Mahmood, E. Dujardin, C. Berger, and W. A. de Heer, Applied Physics Letters **92**, 0119214 (2008).

[29] P. Lauffer, K. V. Emtsev, R. Graupner, T. Seyller, L. Ley, S. A. Reshanov, and H. B. Weber, Physical Review B **77**, 155426 (2008).

[30] T. Nakanishi, M. Koshino, and T. Ando, Phys. Rev. B **82**, 125428 (2010).

[31] A. Mahmood, P. Mallet, and J.-Y. Veuillen, Nanotechnology **23**, 055706 (2012).

[32] E. H. Hwang and S. Das Sarma, Physical Review B **77**, 115449 (2008).

[33] T. Stauber, N. M. R. Peres, and F. Guinea, Physical Review B **76**, 205423 (2007).

[34] B. L. Altshuler and A. Aronov, in *Electron-Electron Interactions in Disordered Systems*, Modern problems in condensed matter science, Vol. 10, edited by A. L. P. M. Efros (North-Holland, Amsterdam, 1985) pp. 1–150.

[35] I. L. Aleiner, B. L. Altshuler, and M. E. Gershenson, Waves in Random Media **9**, 201 (1999).

[36] P. Darancet, N. Wipf, C. Berger, W. A. de Heer, and D. Mayou, Physical Review Letters **101**, 116806 (2008).

[37] A. L. Friedman, J. L. Tedesco, P. M. Campbell, J. C. Culbertson, E. Aifer, F. K. Perkins, R. L. Myers-Ward, J. K. Hite, C. R. Eddy, G. G. Jernigan, and D. K. Gaskill, Nano Letters **10**, 39623965 (2010).

[38] M. M. Parish and P. B. Littlewood, Nature **426**, 162 (2003).

[39] M. M. Parish and P. B. Littlewood, Physical Review B **72**, 094417 (2005).

[40] A. A. Abrikosov, Physical Review B **60**, 4231 (1999).

[41] A. A. Abrikosov, Europhysics Letters **49**, 789 (2000).

[42] The weak localization of an inhomogeneous sample of mono- and bi-layer can be written as $\delta G^{total} = \alpha \delta G^{mono} + \beta \delta G^{bi}$ with $\delta G^{mono} = \delta G_i + \delta G_*$ and $\delta G^{bi} = \delta G_i - \delta G_*$. Due to the fact that the diffusion constant is smaller for the monlayer the amplitude of $\delta G^{mono}$ is smaller than the amplitude of $\delta G^{bi}$. $B_*^{mono} = \frac{\Phi_0}{4\pi D \tau_*^{mono}}$ which gives the magnetic field of the maximum of $\delta G^{mono}$ is larger than $B_*^{bi}$ and the effect of $\delta G^{mono}$ is roughly to enlarge the magnetoresistance. Nevertheless the numerical results of the fits using the bilayer formulae seems correct.

[43] For the sample obtained in UHV, the poor mobility imply that the quantum hall regime is obtained at higher magnetic fields. Thus the linear magnetoresistance regim cannot be reached for the range of magnetic field values used in this study